




Effects of Tin on the Morphological and Electrochemical Properties of Arc-Discharge Nanomaterials

ALEXEY V. ZAIKOVSKII ^{1,4} ANNA A. IURCHENKOVA,²
DMITRIY V. KOZLACHKOV,^{1,2} and EKATERINA O. FEDOROVSKAYA^{2,3}

1.—Kutateladze Institute of Thermophysics SB RAS, 1 Lavrentyev Ave, Novosibirsk, Russia 630090. 2.—Novosibirsk State University, 1 Pirogova Street, Novosibirsk, Russia 630090. 3.—Research Group of Electrochemical Energy Conversion and Storage, Department of Chemistry, School of Chemical Technology, Aalto University, P.O. Box 16100, 00076 Aalto, Finland. 4.—e-mail: lexeyza@gmail.com

Electric arc synthesis enables the fabrication of materials in the form of metal nanoparticles packed into a carbon matrix, which separates the nanoparticles, preventing them from contacting each other, merging, coagulating, or contacting possible reactive environments, thereby stabilizing the nanoparticles. This paper presents the results of studies of the effect of tin on the structure of a composite tin–carbon nanomaterial synthesized by the electric arc method. The concentration of tin affects both the formed carbon structure, changing it from amorphous to graphene-like, and the size of the formed tin nanoparticles. In turn, these structural features affect the electrochemical properties of the synthesized materials used as anodes in lithium-ion batteries. Increasing the tin content increased the specific capacity, but increasing the size of the tin nanoparticles and the rigidity of the carbon matrix decreased the anode material's stability.

INTRODUCTION

Electric arc synthesis involves the evaporation and atomization of electrode material due to the electric arc discharge energy. Subsequent processes of condensation, coagulation, and crystallization form the structure of the nanomaterials. Electric arc synthesis was actively developed after Kratschmer's work on the synthesis of fullerenes¹ during electric arc discharge between graphite electrodes in a helium environment. Adding various metals to the sprayed electrodes allowed the synthesis of composite metal–carbon nanomaterials.^{2,3} These nanomaterials are metallic nanoparticles with carbides on or inside a carbon matrix. Using iron group metals as an additive formed carbon nanotubes.⁴ The nanomaterial structure is influenced not only by the type of additive in the electrode but also by parameters such as the content of the additive in the electrodes, the type and pressure of the buffer gas, and the discharge electrical parameters. For example, using a heavier buffer gas, such as Ar,

decreases the size of the nanoparticles and improves the crystallinity of the carbon structure.⁵ Adding methane to the buffer gas repairs defects in the carbon structure and stimulates the growth of the carbon nanoparticles.⁶ Increasing the pressure of the buffer gas increases the size of the carbon nanoparticles, but their crystallinity deteriorates.⁷ At the same time, increasing the arc discharge current increases the electrode sputtering rate, and the structures acquire more non-equilibrium states.⁸ Using additives such as silicon⁹ and silicon oxide⁸ in the sputtered electrodes forms graphene structures. Earlier, graphene structures were obtained by an electric arc using certain compositions of working gases.^{10,11}

As well as silicon, tin belongs to the IV group of the chemical element table. However, there are only a few studies related to using tin in electric arc synthesis,^{12–14} and other plasma synthesis methods^{15–18} have shown that the synthesized nanomaterial is a composite of tin nanoparticles and carbon material with amorphous and partially graphitized structures. Structural formation processes include

reducing the tin-containing molecules and decomposing carbon-containing gases, forming tin particles coated with a carbon layer.¹⁴

Nanostructured tin is often considered as an anode material for lithium-ion batteries. Using pure lithium anodes in modern Li-ion batteries has not been pursued for safety reasons, since pure lithium forms dendritic structures^{19–21} during the charge–discharge processes, which may short circuit the batteries, causing combustion and explosions. Negative electrodes in commercial Li-ion batteries are currently based on graphite. During battery charging, lithium ions intercalate into graphite and form LiC_6 material.^{22,23} When enriched with lithium ions, the volume of the anode increases by 10%, which does not lead to significant degradation processes. However, batteries with graphite electrodes have a theoretical capacity of only 372 mAhg^{-1} . Tin can theoretically accumulate lithium ions to form a $\text{Li}_{22}\text{Sn}_5$ compound with a theoretical capacity of 994 mAhg^{-1} . However, the volume of the lithium–tin compound during the intercalation of lithium ions increases by almost three times. During lithium intercalation into active material, due to contact with electrolytes, a solid electrolyte interphase (SEI) forms on the surface that, on the one hand, protects the active material from interacting with liquid electrolytes and consuming the active material, and, on the other hand, causes resistance to lithium ion diffusion. Cyclic volume expansion and contraction during the charge–discharge process disrupts the SEI layer, destroys tin anodes, cleaves from the copper contact, and rapidly degrades tin-anode-based batteries. This problem can be partially solved by nanoscaling the tin structures.

During charge–discharge cycles, micron-scale tin particles are destroyed and split off from the copper contact. The battery stability increases as the size of tin nanoparticles decreases;^{24,25} however, a high capacity remains only for a couple of tens of cycles, after which nanosized particles aggregate.²⁴

The transition to nanoscale structures not only helps to mitigate the destruction of the material due to volumetric oscillations but also reduces the path of lithium ion diffusion into the volume of the active material. Nevertheless, the nanostructures must be adsorbed on the surface of the anode and not allowed to aggregate. This has motivated an active research effort to develop a matrix that can adsorb and separate tin particles in the anode. However, the surface of the active materials must be covered with a protective layer, the role of which is played by SEI, and, to prevent its destruction due to the active material volumetric oscillations, the protective layer must show good elasticity. Carbon structures are often investigated as candidate materials for such a matrix and, to date, many studies have demonstrated that tin and carbon nanocomposites have high capacities.^{26–31}

In this study, we used the electric arc method to synthesize tin nanoparticles in a carbon matrix. This method has been previously used to prepare composite Sn/C materials.¹⁴ It is based on electric arc sputtering of Sn/graphite composite electrodes in helium. As a result of the condensation and coagulation processes of the electrode sputtering products, a nanomaterial is formed of spherical tin nanoparticles with an average size of 18 nm packed in a carbon matrix. This study explores the influence of a quantitative composition of sprayed Sn/graphite electrodes on tin and carbon structures in synthesized materials and their electrochemical properties when used as anodes of Li-ion batteries.

EXPERIMENT

Material Synthesis

The materials were obtained using an electric arc reactor that is detailed in Ref. 14. The scheme of the experimental setup is presented on Fig. 1. For the present study, helium was used as the buffer gas with a pressure of 12 Torr. An arc discharge was ignited between a movable graphite cathode with 20 mm diameter (1) and a composite anode (2). The sprayed anode was a graphite cylindrical rod with a diameter and length of 8 and 80 mm, respectively. A cylindrical hole (3) with a diameter and depth of 6 and 50 mm, respectively, was drilled along the rod axis. This hole was densely filled with a powder mixture of graphite (impurity content less than 1 ppm; Carbotec; Russia) and tin (impurities: Sb-200 ppm max, As-1 ppm max, Cu-50 ppm max; ACROS Organics, USA.). The electrical parameters of the discharge were a direct current of 120 A and a voltage of 25 V. This voltage supplied 4 mm of interelectrode spacing. An arc discharge between the electrodes led to the heating of the electrodes, thermal electron emissions, and evaporation of the anode components. A gas–plasma mixture formed between the electrodes, which, upon emerging from the interelectrode space, formed a flow in the form of a non-isothermal turbulent fan-shaped jet. Some of the vaporized components were deposited on the cathode, forming a cathode deposit. The condensation and agglomeration processes in the fan-shaped jet led to the formation of the structure of the materials. The nanomaterial was deposited on the water-cooled wall of the reactor (4).

The composition of the mixture of graphite and metal tin powders filling the cavity in the anode was varied, and was measured by an accurate laboratory balance with an error of less than 5 mg. Experiments were conducted with the carbon–tin mixture with the tin contents of 14 wt.%, 39 wt.%, 60 wt.%, 80 wt.%, and 100 wt.%, and the synthesized materials were labeled T14, T39, T60, T80, and T100, respectively.

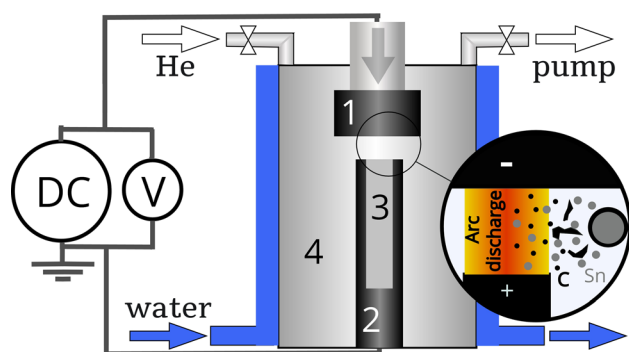


Fig. 1. Schematic of the experimental setup.

Structural Characterisation of the Materials

Transmission electron microscopy (TEM) studies were conducted using a JEM-2200FS electron microscope (JEOL, Japan) operated at 200 kV. The TEM study samples were prepared on a perforated carbon film mounted on a copper grid. A high-angle annular dark-field mode was employed with energy dispersive x-ray (EDX) spectroscopy for EDX mapping.

The EDX of the materials was carried out using an INCA energy attachment (Oxford Instruments Analytical, UK) to a S-3400N scanning electron microscope (Hitachi Science Systems, Japan) with an analyzed square area of $2 \times 2 \text{ mm}^2$.

Raman spectroscopy was conducted using a LabRAM HR Evolution Raman spectrometer instrument (Horiba Jobin Yvon, Germany) using laser radiation with a wavelength of 512 nm.

X-ray diffractometry was carried out with a Bruker D8 Advance instrument (Bruker, Germany) using $\text{CuK}\alpha$ radiation and Bragg–Brentano focusing geometry. Phase analysis was conducted using the ICDD PDF 2 database (Powder Diffraction File PDF-2, International Centre for Diffraction Data, USA, 2009).

Electrochemical Measurements

Battery tests were obtained using a slurry of 85% active materials (Sn/C), 5% SuperP powder (carbon black), and 10% polyvinylidene difluoride. The slurry was dissolved in *N*-methyl pyrrolidone (0.8–1 ml). The resulting suspension was mixed in a Vortex V-1 plus instrument (Biosan, Latvia) for 30 min. The resulting suspension was spread onto a copper foil using a GN-HCM-1025 film coater (Gelco, China) and dried at 80°C under reduced pressure for 16 h. The foil was cut into round electrodes with a diameter of 1.5 cm using a GN-CPM20 manual punching machine (Gelco). The electrodes were placed in an Ar-filled glove box for further assembly of an electrochemical Swagelok-type half-cell (Hohsen, Japan). Approximately 1 mg of active material was on the electrode surface. The electrolyte was 1 M LiPF_6 dissolved in a mixture (volume 1:1) of ethylene carbonate and dimethyl

carbonate (LP30; BASF). Glass fiber filters (GF/A, 0.26 mm; Whatman) were used in the cells as a separator. Charge–discharge experiments were conducted between 0.1 and 2.5 V (versus $\text{Li}|\text{Li}^+$) at a constant current density of $100\text{--}1000 \text{ mAh g}^{-1}$ (galvanostatic mode) at room temperature. The coin cells' rate capabilities were measured with a Neware battery cycler (Neware, China).

RESULTS AND DISCUSSION

Arc Discharge Synthesis

Electric arc synthesis is a common and flexible plasma-chemical method of producing nanomaterials that has been used to obtain various carbon,^{1,4,10} metal,^{2,3} and composite structures.^{2,3,32,33} The external parameters of the arc discharge strongly influence the composition and structure of the synthesized materials. To identify these effects, it is useful to consider the processes that occur during arc discharge.

As previously established,¹⁴ heating evaporates both the tin-containing filling of the electrode cavity and the graphite electrode itself. As a result, a plasma-chemical system forms containing He, Sn, C, C_2 , and C_3 components. The total molar concentration of the remaining components does not exceed 10^{-3} . The movement of the gas system formed from the interelectrode gap is accompanied by cooling, which leads to condensation, agglomeration, and the formation of a nanomaterial structure. As noted in,^{34,35} carbon condensation begins with the formation of nuclei from C_3 molecules that form carbon structures. These carbon structures during further cooling of the gas mixture act as tin condensation centers. Tin condensation begins on the carbon particles in the system.¹⁴ In this case, an increase in the tin content in the sprayed electrode increases the concentration of tin vapor and decreases the concentration of the carbon particles acting as the condensation centers, forming larger-sized tin particles.

Further nanomaterial formation includes the processes of collision and coagulation of the particles. The carbon particle structure has many dangling bonds,⁷ and continuous transformations occur at relatively high temperatures. When the carbon particles interact with each other, a highly disordered structure forms. When interacting with the liquid surface of a tin particle, the carbon particle takes the shape of the surface and forms a graphene-like structure.³⁶ When sufficient carbon material is available to form a continuous coating around the tin particles, the coating separates the tin particles and prevents their fusion and further particle growth.

The subsequent material formation stages include the agglomeration of carbon–tin particles in the gas phase in the chamber volume of the electric arc reactor, and the formed material deposits on the reactor walls.

Structure of the Synthesised Materials

The synthesized materials collected from the water-cooled screen were a loose low-density powder. EDX analysis of the materials showed that the composition contained carbon, tin, and oxygen. The oxygen atom content in the materials varied from 5% to 12% (Fig. 2a), which can be explained by the adsorption of oxygen from air and the formation of oxygen-containing radical groups on the material surface. By deconvoluting the oxygen signal from the EDX spectra, the tin atom content in the materials varied from 5% to 65%, and carbon atom content varied from 95% to 35% (Fig. 2b).

A TEM study of the materials (Fig. 3) showed that they consist of spherical tin particles and a carbon structure. Tin nanoparticles are mainly coated with a carbon layer. However, uncovered tin nanoparticles are also observed in the T80 and T100 materials. If a tin nanoparticle is not covered with a carbon matrix, its surface may oxidize upon contact with air during storage and transportation of the material. Therefore, some nanoparticles may acquire a core-shell structure with a tin core and a tin oxide shell (Fig. 3g), which was also discovered in Ref. 13. In this case, the tin oxide shell has an amorphous structure. XRD analysis (Fig. 4a) showed that the synthesized materials have crystal structures of graphite-2H with a $P63/mmc$ space group (PDF card: 00-041-1487) and tin with a $I41/amd$ space group (PDF card: 04-004-7747). Moreover, the content of the material crystalline structure was calculated by the reference intensity ratio method which showed the tin content varying from 1 wt.% to 85 wt.% and the graphite content varied from 99 wt.% to 15 wt.% (Fig. 4b). The size distributions of the tin nanoparticles are well described by a log-normal distribution, while, for the T14 and T100 materials, the distributions are bimodal (Fig. 3). The average size of the tin nanoparticles increases with the increasing tin concentration from 7.5 nm to 23.3 nm (Fig. 3f).

Carbon in the materials is present in the form of amorphous globules and graphitized shells around the tin nanoparticles. Empty cavities with graphitized walls are also observed in the carbon materials.

The Raman spectra of the synthesized materials (Fig. 5a) contain peaks that provide information about the carbon structure. The most intense D peaks ($\sim 1350\text{ cm}^{-1}$) are associated with the breathing vibrations of the rings in the graphite structure that exist only at the boundaries and structural defects, while the G peak ($\sim 1590\text{ cm}^{-1}$) is related to the vibrations associated with the stretching of the C-C bonds of the sp^2 -hybridized carbon atoms in hexagonal rings and linear chains.³⁷ Close to $\sim 1620\text{ cm}^{-1}$, a Gs peak may also exist that is associated with an imperfection of the carbon structure, but its position on the edge of the much more intense G peak prevents its clear identification. The 2D ($\sim 2690\text{ cm}^{-1}$), D + Gs ($\sim 2930\text{ cm}^{-1}$), and 2Gs ($\sim 3230\text{ cm}^{-1}$) peaks are the overtones of the main peaks.³⁸ The peak ID/IG and I2D/IG intensity ratios allow us to characterize the imperfection degree of the carbon structure.³⁹ These coefficients are shown for different materials in Fig. 5b, and indicate that an increase in the tin concentration forms a carbon material with a more graphenized structure. The ID/IG ratio value changes by no more than 37% at varying tin concentrations. The I2D/IG ratio value increases by more than 3 times as the tin concentration increases from T14 to T100. The I2D/IG reaches a maximum value of 0.5 for T100, which corresponds to multilayer graphene.⁴⁰ The D band appears due to the presence of defects and boundaries in the graphite material. However, the process leading to the appearance of the 2D band competes with the processes leading to the appearance of the D band, and its intensity increases as the graphene structure improves. Thus, an increase in the concentration of tin in the sputtered electrode forms a material with carbon with stronger graphene features, which can also be observed in the TEM images of the T100 material (Fig. 3e).

Electrochemical Analysis of the Synthesised Materials

Electrochemical properties of synthesised materials were investigated in half cells (versus Li/Li⁺). The carbon material (C12) obtained in our previous research⁷ under the same arc discharge conditions

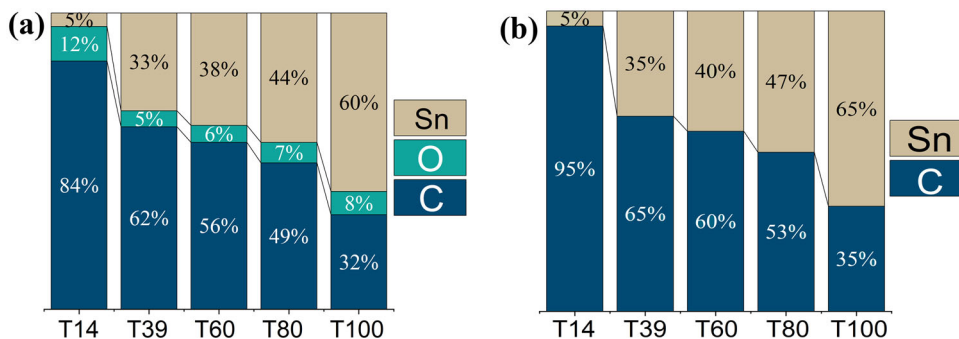


Fig. 2. (a) Atom contents of the synthesized materials; (b) atom proportions of tin and carbon in the materials.

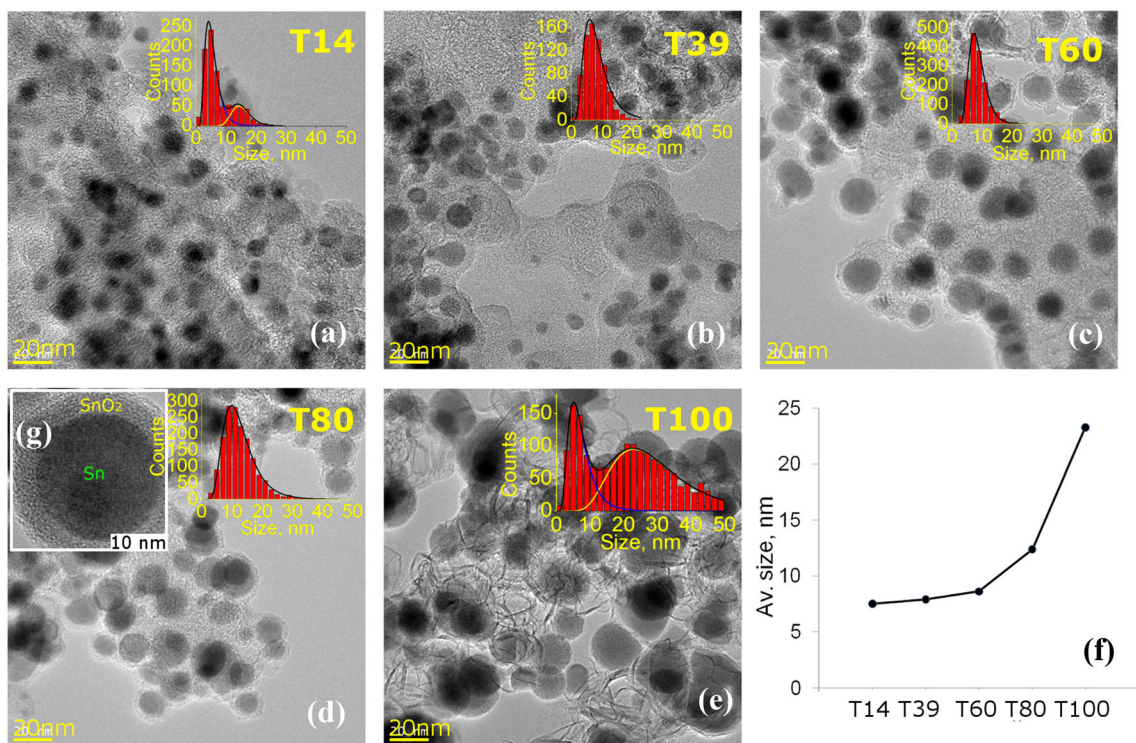


Fig. 3. TEM images of T14 (a), T39 (b), T60 (c), T80 (d), T100 (e) and dependences of the average size of tin nanoparticles for different materials (f), and core-shell nanoparticle Sn@SnO₂.

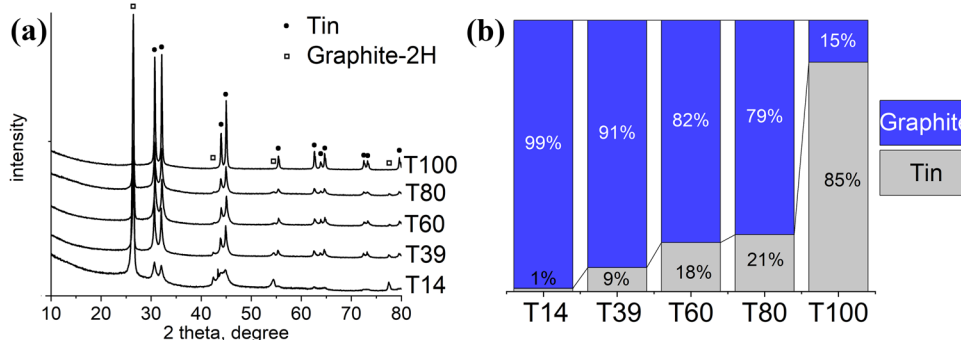


Fig. 4. XRD spectra (a) and crystalline mass composition (b) of the materials.

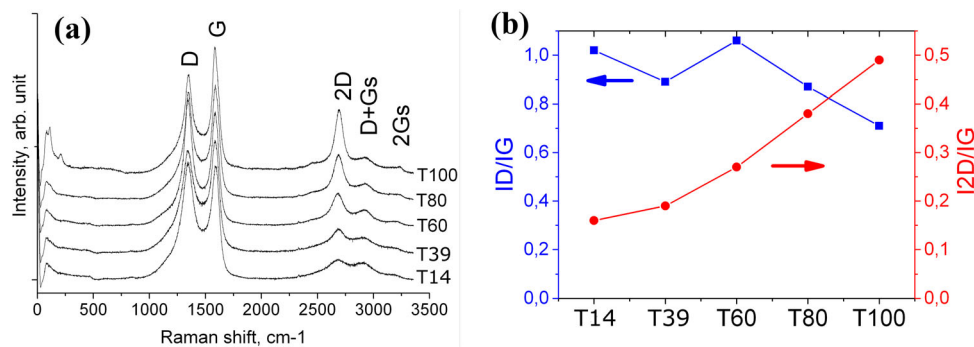


Fig. 5. Raman spectra (a) and ID/IG and I2D/IG ratios (b) for different synthesised materials.

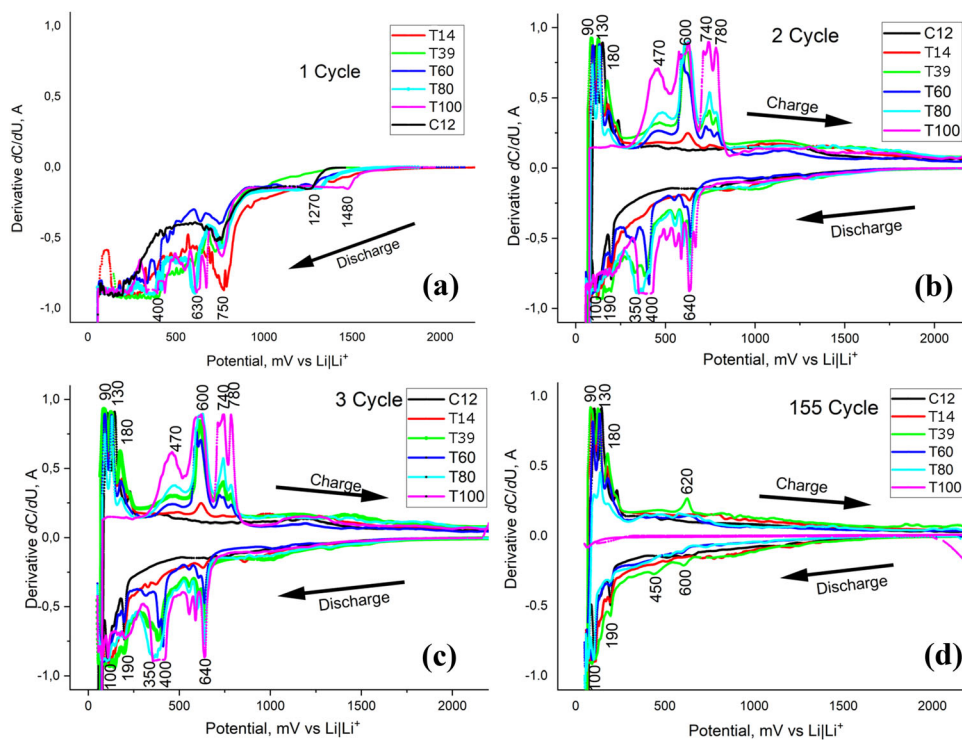


Fig. 6. dQ/dV plots for 1st (a), 2nd (b), 3rd (c), and 155th (d) cycles for different materials.

used in this work was also studied. Figure 6 shows the differential capacity (dQ/dV)⁴¹ plots for 1st, 2nd, 3rd, and 155th cycles. The first cycle corresponds to the discharge of the electrochemical cell. For material C12, the plot shows anodic peaks in the 750- and 1270-mV regions, which correspond to irreversible reactions on the anode material and the formation of a SEI layer. These peaks do not appear in further cycles. In materials containing tin, the plots of the first cycle also have anodic peaks in the 400-mV and 630-mV regions corresponding to the interaction processes of nanosized tin with lithium;⁴² these peaks are also observed in the next cycles. In the second and third cycles, cathodic peaks are clearly seen in the 470-mV, 600-mV, 740-mV, and 780-mV regions. These peaks correspond to the formation of tin–lithium compounds.^{43,44} Moreover, these peaks are absent in the pure carbon material C12, and, as the amount of tin in the materials increases, their intensity increases. The anodic peak intensity in the 350-mV, 400-mV, and 640-mV regions also increases as the amount of tin increases. In the plots for cycle 155, only faint signs of a tin cathodic peak in the 620-mV region and anodic peaks in the 450-mV and 600-mV regions remain. Cathodic peaks in the 90-mV, 130-mV, and 180-mV regions and anodic peaks in the 100-mV and 190-mV regions practically coincide with the peaks of the carbon material C12, indicating that they correspond to the interaction–deintercalation processes of lithium within the carbon structure. There is also some divergence in the plots of

different materials on the 155th cycle. Thus, for T100, the discharge and charge curves practically coincide, indicating the material's low capacity. As the amount of tin decreases, the carbon peak intensity slightly increases, with the exception of T39, which has maximum peak intensities that exceed even the peaks of the C12. This indicates that the carbon structure in materials synthesized with a lower tin content is more stable in lithium intercalation–deintercalation processes.

Figure 7a shows the specific capacities of the different anode materials at various current densities, while Fig. 7b shows the results of the averaging of the specific capacitance of the materials at various current densities. For this plot, the results obtained in the first cycles were excluded because the formation of the SEI layer had a strong effect on the material behavior during the first several cycles. The presence of tin increases the specific capacity compared to a pure carbon material. The increase in the tin concentration increases the specific capacity during the first cycles at a current density of 100 mA g^{-1} , and reaches a maximum value of 461 mAh g^{-1} (charge) and 483 mAh g^{-1} (discharge) in the T60 material, which is almost 100 mAh g^{-1} more than the theoretical maximum capacity for graphite materials (372 mAh g^{-1}). The specific capacity value decreases in the T80 material and declines sharply to 159 mAh g^{-1} (charge) and 162 mAh g^{-1} (discharge) in the T100 material. The dQ/dV plots (Fig. 6) indicate that this happens due to the rapid

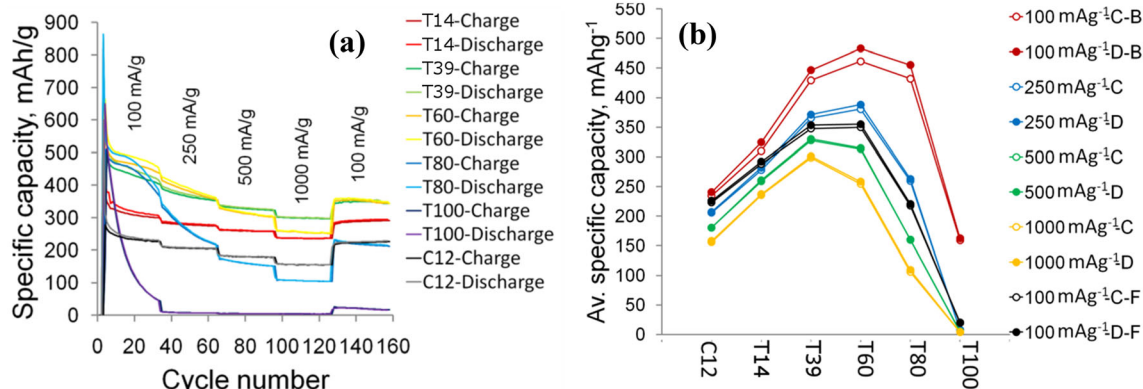


Fig. 7. (a) Specific capacity of Li-ion batteries with synthesized anode materials at various current densities; (b) average values of the specific capacitance at varying cycling currents in the different materials.

decrease in these material-specific capacities which occur due to their rapid degradation. The increase in the charge–discharge current decreases the specific capacitance, while, in the T60 and T80 materials with larger tin nanoparticles and a more structured carbon matrix, the decrease in the capacity occurs faster than in the T14 and T39 materials with smaller tin nanoparticles and more defective carbon structures. The dQ/dV plots (Fig. 6) also show that the carbon peaks are more stable in materials synthesized with a lower tin content and have a more defective carbon structure. Thus, the maximum current density of 1000 mA g^{-1} and the maximum capacity of 298 mAh g^{-1} (charge) and 301 mAh g^{-1} (discharge) are already obtained for the T39 material. However, when the current density of 100 mA g^{-1} is used again in the last cycles, the capacitances of the T39 and T60 materials are almost the same at 353 mAh g^{-1} and 355 mAh g^{-1} (charge), and 348 mAh g^{-1} and 350 mAh g^{-1} (discharge), respectively. Thus, the depth of the lithium ion diffusion into the volume of the carbon–tin material depends on the current density. The difference between the specific capacitance values at a current density of 100 mA g^{-1} in the first and last cycles increases as the material tin concentration increases, with the exception of T100, for which the initial specific capacity has a low value of 159 mAh g^{-1} (charge) and 162 mAh g^{-1} (discharge) and rapidly decreases to a very low 19 mAh g^{-1} (charge) and 20 mAh g^{-1} (discharge). These results indicate that the material stability decreases as the tin content increases.

Intercalation of lithium ions into the tin structure expands the particle volume. The carbon structure surrounding the tin particles is also forced to expand. The materials with a lower tin content consist of smaller tin nanoparticles and a more defective carbon structure. Defects make the carbon matrix more elastic and the Sn/C material more stable during volume expansion and contraction cycles, which are also confirmed by the results of the

dQ/dV analysis. However, the materials with a high tin content consist of larger tin nanoparticles and a more rigid graphenized carbon structure which is more prone to destruction during the nanoparticle cyclical expansion–contraction. Moreover, the initially synthesised T80 and T100 materials already contained some tin particles uncovered by the carbon structure. Due to the destruction of the carbon shell surrounding the tin particles, the bare surface of the tin reacts with the electrolytes, degrading the material and correspondingly decreasing the battery specific capacity. However, the T14, T39, and T60 materials show a specific capacity higher than those of commercial anode materials which are graphite materials, ranging from 330 to 430 mAh cm^{-3} or from 170 to 20 mAh g^{-1} .⁴⁵

After 160 cycles, two batteries with T39 material were disassembled in a charged (Fig. 8a) and discharged (Fig. 8b) state. TEM analysis of the anode materials was conducted. Due to the low density of the Sn–Li compound in the charged state, the material did not have sufficient contrast for the unambiguous identification of the particles against the carbon matrix background in the bright-field mode of the microscope. However, dark-field analysis and EDX mapping showed that tin is distributed over the carbon globule surface. Analysis of the material in the discharged state shows the presence of tin nanoparticles on the carbon, with an average particle size of 2.7 nm . The average size of the tin nanoparticles in the T39 material is 7.9 nm . The decrease in the average size is associated with the destruction of large tin nanoparticles during cycling.

CONCLUSION

Arc sputtering of composite tin–graphite electrodes forms a nanomaterial with a structure consisting of spherical tin nanoparticles encapsulated in a carbon matrix.

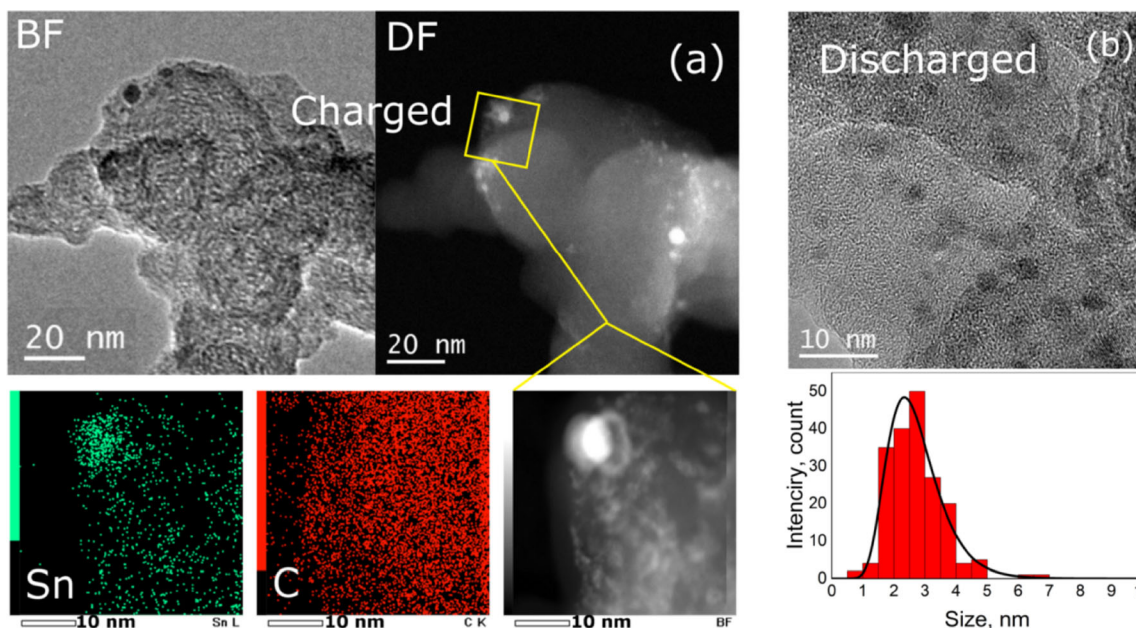


Fig. 8. (a) TEM analysis and EDX mapping of the material in the charged state; (b) TEM analysis and size distribution of the tin nanoparticles in the discharged material.

Increasing the tin concentration in the composition of the sprayed electrode changes the internal arc discharge parameters, which affects the parameters of the condensation process and the parameters of the formation of the tin–carbon nanomaterial structure. This leads to changes in several structural features of the materials. First, increasing the tin concentration in the sputtering electrodes increases the tin content in the synthesized structures. Second, the sizes of the formed tin nanoparticles increase. Third, the carbon structure surrounding the tin nanoparticles has a greater structural order, approaching that of multilayer graphene.

When synthesized materials are used as anode materials in lithium-ion batteries, the material-specific capacity and stability are influenced by several factors such as the tin content in the materials, the size of the tin nanoparticles, and the structure of the carbon matrix surrounding the tin nanoparticles. Increasing the tin content in the materials increases the battery-specific capacity, accompanied by an increase in the size of the tin nanoparticles and the structure of the carbon matrix which negatively affects the material stability during the cycling processes. The combination of these factors leads to an optimal performance obtained for materials consisting of 35–40 wt.% tin nanoparticles with an average size of 7–9 nm covered by a carbon matrix. These materials show a maximum capacity after prolonged cycling. Moreover, due to the change in the depth of the lithium ion diffusion in the tin–carbon structure, increasing the cycling current shifts the optimal material structure toward tin nanoparticles with smaller sizes.

ACKNOWLEDGEMENTS

The study of the arc discharge synthesis was carried out under state contract with IT SB RAS (AAAA-A17-117071760008-0). Morphological and structural characterization of the materials and the electrochemical study were supported by the Russian Science Foundation (Project No. 20-79-00085).

CONFLICT OF INTEREST

On behalf of all the authors, the corresponding author states that there is no conflict of interest.

REFERENCES

1. W. Krätschmer, L.D. Lamb, K. Fostiropoulos, and D.R. Huffman, *Nature* 347, 354 (1990). <https://doi.org/10.1038/47354a0>.
2. Y. Saito, M. Okuda, T. Yoshikawa, A. Kasuya, and Y. Nishina, *J. Phys. Chem. Solids* 98, 6696 (1994). <https://doi.org/10.1021/j100078a008>.
3. J.H.J. Scott and S.A. Majetich, *Phys. Rev. B* 52, 12564 (1995). <https://doi.org/10.1103/PhysRevB.52.12564>.
4. S. Iijima, *Nature* 354, 56 (1991). <https://doi.org/10.1038/354056a0>.
5. M. Reza Sanaee, S. Chaitoglou, N. Aguiló-Aguayo, and E. Bertran, *Appl. Sci.* 7, 26 (2017). <https://doi.org/10.3390/ap7101026>.
6. R. Hu, M. Alexandru Ciolan, X. Wang, and M. Nagatsu, *Nanotechnology* 27, 335602 (2016). <https://doi.org/10.1088/0957-4484/27/33/335602>.
7. A.V. Zaikovskii and S.A. Novopashin, *Phys. Status Solidi A* 214, 1700142 (2017). <https://doi.org/10.1002/pssa.201700142>.
8. A.V. Zaikovskii, T.Y. Kardash, B.A. Kolesov, and O.A. Nikolaeva, *Phys. Status Solidi A* 216, 1900079 (2019). <https://doi.org/10.1002/pssa.201900079>.
9. D.V. Smovzh, I.A. Kostogrud, S.Z. Sakhapov, A.V. Zaikovskii, and S.A. Novopashin, *Carbon* 112, 97 (2017). <https://doi.org/10.1016/j.carbon.2016.10.094>.

10. K.S. Subrahmanyam, L.S. Panchakarla, A. Govindaraj, and C.N.R. Rao, *J. Phys. Chem. C* 113, 4257 (2009). <https://doi.org/10.1021/jp900791y>.
11. Y. Chen, H. Zhao, L. Sheng, L. Yu, K. An, J. Xu, and X. Zhao, *Chem. Phys. Lett.* 538, 72 (2012). <https://doi.org/10.1016/j.cplett.2012.04.020>.
12. W. Xiaohui, L. Zhiliang, Z. Jie, L. Xingguo, and S. Zujin, *J. Mat. Chem. A* 5, 13769 (2017). <https://doi.org/10.1039/c7ta03323k>.
13. T.Y. Kardash, E.A. Derevyannikova, E.M. Slavinskaya, A.I. Stadnichenko, V.A. Maltsev, A.V. Zaikovskii, S.A. Novopashin, A.I. Boronin, and K.M. Neyman, *Front. Chem.* 7, 114 (2019). <https://doi.org/10.3389/fchem.2019.00114>.
14. A. Zaikovskii, S. Novopashin, V. Maltsev, T. Kardash, and I. Shundrina, *RSC Adv.* 9, 36621 (2019). <https://doi.org/10.1039/C9RA05485E>.
15. H. Lee, S.H. Park, S.J. Kim, Y.K. Park, B.H. Kim, and S.C. Jung, *Microelectron. Eng.* 126, 153 (2014). <https://doi.org/10.1016/j.mee.2014.07.014>.
16. G. Saito, C. Zhu, and T. Akiyama, *Adv. Powder Technol.* 25, 728 (2014). <https://doi.org/10.1016/j.apt.2013.11.001>.
17. Z. Kelgenbaeva, E. Omurzak, H. Ihara, C. Iwamoto, S. Sulaimankulova, and T. Mashimo, *Phys. Status Solidi A* 212, 2951 (2015). <https://doi.org/10.1002/pssa.201532502>.
18. M. Shariat, R. Shaida, M. Karimpour, and M. Molaei, *Mater. Res. Exp.* 6, 015019 (2018). <https://doi.org/10.1088/2053-1591/aae5bc>.
19. Y. He, X. Ren, Y. Xu, M.H. Engelhard, X. Li, J. Xiao, J. Liu, J.G. Zhang, W. Xu, and C. Wang, *Nat. Nanotechnol.* 14, 1042 (2019). <https://doi.org/10.1038/s41565-019-0558-z>.
20. L. Frenck, G.K. Sethi, J.A. Maslyn, and N.P. Balsara, *Front. Energy Res.* 7, 115 (2019). <https://doi.org/10.3389/ferng.2019.00115>.
21. K.N. Wood, E. Kazyak, A.F. Chadwick, K.H. Chen, J.G. Zhang, K. Thornton, N.P. Dasgupta, and A.C.S. Cent, *Science* 2, 790 (2016). <https://doi.org/10.1021/acscentsci.6b00260>.
22. D. Allart, M. Montaru, and H. Gualous, *J. Electrochem. Soc.* 165, A380–A387 (2018). <https://doi.org/10.1149/2.1251802jes>.
23. D. Martin, S. Martin, and R. Markus, *J. Power Sources* 353, 58 (2017). <https://doi.org/10.1016/j.jpowsour.2017.03.152>.
24. L. Wang, M. Feyngenson, M.C. Aronson, and W.Q. Han, *J. Phys. Chem. C* 114, 14697 (2010). <https://doi.org/10.1021/jp101852y>.
25. K. Kravchik, L. Protesescu, M.I. Bodnarchuk, F. Krumeich, M. Yarema, M. Walter, C. Guntlin, and M.V. Kovalenko, *J. Am. Chem. Soc.* 135, 14697 (2013). <https://doi.org/10.1021/jp101852y>.
26. W. Xiaohui, L. Zhiliang, Z. Jie, L. Xingguo, and S. Zujin, *J. Mater. Chem. A* 5, 13769 (2017). <https://doi.org/10.1039/C7TA03323K>.
27. J.Q.C. He, N. Zhao, Z. Wang, C. Shi, E.Z. Liu, and J. Li, *ACS Nano* 8, 1728 (2014). <https://doi.org/10.1021/nn406105n>.
28. Y. Yu, L. Gu, C. Wang, A. Dhanabalan, and P.A. Aken, *J. Maier. Angew. Chem. Int. Ed.* 48, 6485 (2009). <https://doi.org/10.1002/anie.200901723>.
29. S. Li, Z. Wang, J. Liu, L.Y. Yang, Y. Guo, L. Cheng, M. Lei, and W. Wang, *ACS Appl. Mater. Interfaces* 8, 19438 (2016). <https://doi.org/10.1021/acsami.6b04736>.
30. F. Cheng, W.C. Li, J.N. Zhu, W.P. Zhang, and A.H. Lu, *Nano Energy* 19, 486 (2016). <https://doi.org/10.1016/j.nanoen.2015.10.033>.
31. C. Cui, X. Liu, N. Wu, and Y. Sun, *Mater. Lett.* 143, 35 (2015). <https://doi.org/10.1016/j.matlet.2014.12.055>.
32. J. Jiao, S. Seraphin, X. Wang, and J.C. Withers, *J. Appl. Phys.* 80, 103 (1996). <https://doi.org/10.1063/1.362765>.
33. C. Guerret-Piecourt, Y.L. Bouar, A. Lolsaut, and H. Pascard, *Nature* 372, 761 (1994). <https://doi.org/10.1038/372761a0>.
34. S. Yatom, A. Khrabry, J. Mitrani, A. Khodak, I. Kaganovich, V. Vekselman, B. Stratton, and Y. Raites, *MRS Commun.* 8, 842 (2018). <https://doi.org/10.1557/mrc.2018.91>.
35. P. Kappler, P. Ehrburger, J. Lahaye, and J.B. Donnet, *J. Appl. Phys.* 50, 308 (1979). <https://doi.org/10.1063/1.3256660>.
36. J. Liu and L. Fu, *Adv. Mater.* 31, 1800690 (2018). <https://doi.org/10.1002/adma.201800690>.
37. A.C. Ferrari and J. Robertson, *Phys. Rev. B* 64, 075414 (2001). <https://doi.org/10.1103/PhysRevB.64.075414>.
38. E.J. Heller, Y. Yang, L. Kocia, W. Chen, S. Fang, M. Borunda, and E. Kaxiras, *ACS Nano* 10, 2803 (2016). <https://doi.org/10.1021/acsnano.5b07676>.
39. A.C. Ferrari and J. Robertson, *Phys. Rev. B* 61, 14095 (2000). <https://doi.org/10.1103/PhysRevB.61.14095>.
40. X. Dong, P. Wang, W. Fang, C.Y. Su, Y.H. Chen, L.J. Li, and P. Chen, *Carbon* 49, 3672 (2011). <https://doi.org/10.1016/j.carbon.2011.04.069>.
41. A.J. Smith and J.R. Dahn, *J. Electrochem. Soc.* 159, A290 (2012). <https://doi.org/10.1149/2.076203jes>.
42. N. Zhang, Y. Wang, M. Jia, Y. Liu, J. Xu, L. Jiao, and F. Cheng, *Chem. Commun.* 54, 1205 (2018). <https://doi.org/10.1039/c7cc09095a>.
43. R.A. Huggins, *J. Power Sources* 81, 13 (1999). [https://doi.org/10.1016/s0378-7753\(99\)00124-x](https://doi.org/10.1016/s0378-7753(99)00124-x).
44. J.H. Kim, G.F. Jeong, Y.W. Kim, H.J. Sohn, C.W. Park, and C.K. Lee, *J. Electrochem. Soc.* 150, A1544 (2003). <https://doi.org/10.1149/1.1617302>.
45. N. Nitta, F. Wu, J.T. Lee, and G. Yushin, *Mater. Today* 18, 252 (2015). <https://doi.org/10.1016/j.mattod.2014.10.040>.